



## Nanoscale structural investigation of $\text{Zn}_{1-x}\text{Mg}_x\text{O}$ alloy films on polar and nonpolar ZnO substrates with different Mg contents

Xin Liang(梁信), Hua Zhou(周华), Hui-Qiong Wang(王惠琼), Lihua Zhang(张丽华), Kim Kisslinger, and Junyong Kang(康俊勇)

**Citation:** Chin. Phys. B, 2021, 30 (9): 096107. DOI: 10.1088/1674-1056/ac11e1

Journal homepage: <http://cpb.iphy.ac.cn>; <http://iopscience.iop.org/cpb>

**What follows is a list of articles you may be interested in**

---

### Crystal structure and magnetic properties of disordered alloy $\text{ErGa}_{3-x}\text{Mn}_x$

Cong Wang(王聪), Yong-Quan Guo(郭永权), Shuo-Wang Yang(杨硕望)

Chin. Phys. B, 2019, 28 (8): 086101. DOI: 10.1088/1674-1056/28/8/086101

### Studies on the nucleation of MBE grown III-nitride nanowires on Si

Yanxiong E(鄂炎雄), Zhibiao Hao(郝智彪), Jiadong Yu(余佳东), Chao Wu(吴超), Lai Wang(汪莱), Bing Xiong(熊兵), Jian Wang(王健), Yanjun Han(韩彦军), Changzheng Sun(孙长征), Yi Luo(罗毅)

Chin. Phys. B, 2017, 26 (1): 016103. DOI: 10.1088/1674-1056/26/1/016103

### Temperature dependence of surface and structure properties of ZnCdO film

Lei Hong-Wen, Yan Da-Wei, Zhang Hong, Wang Xue-Min, Yao Gang, Wu Wei-Dong, Zhao Yan

Chin. Phys. B, 2014, 23 (12): 126104. DOI: 10.1088/1674-1056/23/12/126104

### Quasi-homoepitaxial GaN-based blue light emitting diode on thick GaN template

Li Jun-Ze, Tao Yue-Bin, Chen Zhi-Zhong, Jiang Xian-Zhe, Fu Xing-Xing, Jiang Shuang, Jiao Qian-Qian, Yu Tong-Jun, Zhang Guo-Yi

Chin. Phys. B, 2014, 23 (1): 016101. DOI: 10.1088/1674-1056/23/1/016101

### Detection of Fe 3d electronic states in valence band and magnetic properties of Fe-doped ZnO film

Chen Tie-Xin, Cao Liang, Zhang Wang, Han Yu-Yan, Zheng Zhi-Yuan, Xu Fa-Qiang, Ibrahim Kurash, Qian Hai-Jie, Wang Jia-Ou

Chin. Phys. B, 2013, 22 (2): 026101. DOI: 10.1088/1674-1056/22/2/026101

---

# Nanoscale structural investigation of $\text{Zn}_{1-x}\text{Mg}_x\text{O}$ alloy films on polar and nonpolar ZnO substrates with different Mg contents\*

Xin Liang(梁信)<sup>1</sup>, Hua Zhou(周华)<sup>2,†</sup>, Hui-Qiong Wang(王惠琼)<sup>1,3,‡</sup>, Lihua Zhang(张丽华)<sup>4</sup>,  
Kim Kisslinger<sup>4</sup>, and Junyong Kang(康俊勇)<sup>1</sup>

<sup>1</sup>Key Laboratory of Semiconductors and Applications of Fujian Province, Collaborative Innovation Center for Optoelectronic Semiconductors and Efficient Devices, Department of Physics, Xiamen University, Xiamen 361005, China

<sup>2</sup>School of Physics, Shandong University, Jinan 250100, China

<sup>3</sup>Department of Physics, Xiamen University Malaysia, Sepang 43900, Selangor, Malaysia

<sup>4</sup>Center for Functional Nanomaterials, Brookhaven National Laboratory, Upton, New York 11973, USA

(Received 6 April 2021; revised manuscript received 21 June 2021; accepted manuscript online 7 July 2021)

$\text{Zn}_{1-x}\text{Mg}_x\text{O}$  alloy films are important deep ultraviolet photoelectric materials. In this work, we used plasma-assisted molecular beam epitaxy to prepare  $\text{Zn}_{1-x}\text{Mg}_x\text{O}$  films with different magnesium contents on polar (0001) and nonpolar (10 $\bar{1}$ 0) ZnO substrates. The nanoscale structural features of the grown alloy films as well as the interfaces were investigated. It was observed that the cubic phases of the alloy films emerged when the Mg content reached 20% and 37% for the alloy films grown on the (0001) and (10 $\bar{1}$ 0) ZnO substrates, respectively. High-resolution transmission electron microscopy images revealed cubic phases without visible hexagonal phases for the alloy films with more than 70% magnesium, and the cubic phases exhibited three-fold and two-fold rotations for the alloy films on the polar (0001) and nonpolar (10 $\bar{1}$ 0) ZnO substrates, respectively. This work aims to provide references for monitoring the  $\text{Zn}_{1-x}\text{Mg}_x\text{O}$  film structure with respect to different substrate orientations.

**Keywords:**  $\text{Zn}_{1-x}\text{Mg}_x\text{O}$  films, molecular beam epitaxy, phase separation, transmission electron microscopy

**PACS:** 61.72.uj, 05.70.Fh, 07.30.Kf

**DOI:** 10.1088/1674-1056/ac11e1

## 1. Introduction

The development of technology requires the ability to monitor the optical band gap range of many optoelectronic materials from violet light waves to ultraviolet light waves. Band-gap engineering is an effective strategy to solve this problem. A common method is to alloy ZnO with MgO. ZnO is a II–VI direct band gap semiconductor with a band gap of 3.37 eV and a large exciton binding energy of 60 meV at room temperature, and can be crystallized into a hexagonal wurtzite structure ( $a = 3.25 \text{ \AA}$ ,  $c = 5.20 \text{ \AA}$ ).<sup>[1,2]</sup> MgO is a typical cubic structure with an optical band gap of approximately 7.8 eV.<sup>[3]</sup> This alloy material ( $\text{Zn}_{1-x}\text{Mg}_x\text{O}$ ) can achieve tunable bandgaps from 3.37 eV to 7.8 eV.<sup>[4]</sup> Therefore,  $\text{Zn}_{1-x}\text{Mg}_x\text{O}$  alloy films have broad potential applications in deep ultraviolet light-emitting diodes, solar-blind photodetectors, etc.<sup>[5,6]</sup> Nonetheless, these optoelectronic devices require a band gap larger than 4.0 eV for a  $\text{Zn}_{1-x}\text{Mg}_x\text{O}$  film with an Mg content of more than 45%. This requirement often results in the formation of mixed-phase structures in the  $\text{Zn}_{1-x}\text{Mg}_x\text{O}$  films.<sup>[7,8]</sup> However, the mixed phase is unstable due to the large difference in the phase structures between ZnO and MgO, especially when the Mg content is between 37% and 62%.<sup>[9,10]</sup> The unstable mixing phase in alloy films is usually accompanied by numerous grain boundaries.<sup>[11,12]</sup>

Understanding these complex boundary structures is a key step to improve the stability of the mixing phase and the optoelectronic performance of this semiconductor, especially at a high Mg content of more than 62%.

On the other hand, integrating semiconductor ZnO with cubic materials that have unique properties has recently been increasingly studied.<sup>[13,14]</sup> For example, novel optoelectronics and memory devices have been fabricated by combining  $\text{SrTiO}_3$ ,<sup>[15]</sup> which exhibits an abundance of physical properties, such as two-dimensional (2D) electron gas,<sup>[16]</sup> ferroelectricity,<sup>[17]</sup> magnetism,<sup>[18]</sup> and superconductivity.<sup>[19]</sup> Similarly, integrating perovskite  $\text{Pb}(\text{Zr,Ti})\text{O}_3$ ,<sup>[20]</sup>  $\text{SrRuO}_3$ ,<sup>[21]</sup> and  $\text{BiFeO}_3$ <sup>[22]</sup> with wurtzite ZnO promotes faster response time and the production of more efficient field-effect transistors or resistance random access memory devices. In thermal equilibrium, ZnO is hexagonal wurtzite, while the crystal structure of MgO is cubic rock salt. For higher Mg ( $x > 0.5$ ) concentrations, cubic  $\text{Zn}_{1-x}\text{Mg}_x\text{O}$  with a band gap energy higher than 5 eV has been obtained, as well as a direct energy band structure.<sup>[23–25]</sup> Therefore, this material has high potential application values due to the perspective of developing optical functions in the deep ultraviolet region.

MgO has a representative simple cubic structure and is widely used as a buffer layer on a wurtzite structure

\*Project supported by the National Natural Science Foundation of China (Grant No. 11804050).

†Corresponding author. E-mail: [zhouhua2018@sdu.edu.cn](mailto:zhouhua2018@sdu.edu.cn)

‡Corresponding author. E-mail: [hqwang@xmu.edu.cn](mailto:hqwang@xmu.edu.cn)

© 2021 Chinese Physical Society and IOP Publishing Ltd

<http://iopscience.iop.org/cpb> <http://cpb.iphy.ac.cn>

substrate.<sup>[14,26,27]</sup> Therefore, the homoepitaxy of the cubic  $\text{Zn}_x\text{Mg}_{1-x}\text{O}$  film on the wurtzite ZnO substrate provides a template for studying the boundary structure and interfacial structure between the cubic film and wurtzite substrate. To address these issues, we propose a  $\text{Zn}_{1-x}\text{Mg}_x\text{O}$  alloy film epitaxy on ZnO substrates with different orientations and investigate the films and interfacial structures. In this work,  $\text{Zn}_{1-x}\text{Mg}_x\text{O}$  alloy films were grown on polar *c*-plane (0001) ZnO and non-polar *m*-plane (10 $\bar{1}$ 0) substrates by plasma-assisted molecular beam epitaxy (MBE). The Mg contents were examined by energy dispersive spectroscopy (EDS). The film and interfacial structures were revealed through x-ray diffraction (XRD) and transmission electron microscopy (TEM).

## 2. $\text{Zn}_{1-x}\text{Mg}_x\text{O}$ films preparation

MBE has the advantages of ultra-high vacuum growth environment, low film growth temperature, controllable growth process, and so on. The process of film growth by MBE involves the adsorption, decomposition, nucleation, and desorption of atoms or molecules, which is a kinetic process. So it can be used to prepare epitaxial film layers that cannot be prepared by traditional thermal equilibrium growth methods. Therefore, we used MBE to deposit  $\text{Zn}_{1-x}\text{Mg}_x\text{O}$  thin films. A series of  $\text{Zn}_{1-x}\text{Mg}_x\text{O}$  films were grown by MBE on (0001)- and (10 $\bar{1}$ 0)-ZnO substrates. Before growth, all substrates were treated in the growth chamber by annealing at 350 °C for 60 min in an oxygen plasma with an O partial pressure of  $1 \times 10^{-3}$  Pa and a power of 250 W. The  $\text{Zn}_{1-x}\text{Mg}_x\text{O}$  films were then deposited for 2 h, with the oxygen partial pressure maintained at  $1 \times 10^{-3}$  Pa and the power of the oxygen plasma changed to 200 W, while the substrate temperature was increased to 400 °C. At the same time, magnesium and zinc beams were injected toward the substrate with the adjustment of the temperature of the beam source furnace to tune the Mg/Zn ratio. The as-grown films were then annealed for 30 min with the substrate temperature maintained at 400 °C (O partial pressure  $\sim 1 \times 10^{-3}$  Pa, O plasma power  $\sim 200$  W) to reduce defects.

## 3. XRD results and discussion

To obtain the Mg content ( $x$ ) and Zn content ( $1-x$ ) in the  $\text{Zn}_{1-x}\text{Mg}_x\text{O}$  films with different alloy compositions, which was achieved through the control of the Mg:Zn flux ratios, we characterized the Mg and Zn concentrations by EDS (Thermo Fisher, Czech Republic). Here, we defined the concentration of Mg plus Zn to be 100%. Figure 1 shows the Mg contents of the  $\text{Zn}_{1-x}\text{Mg}_x\text{O}$  films grown on the *c*-plane (0001) ZnO and the *m*-plane (10 $\bar{1}$ 0) ZnO. The Mg content  $x$  nearly linearly increases from approximately 19% to 75% with an increasing temperature of the magnesium beam source furnace (Mg

source temperature) from 340 °C to 400 °C, and the Zn content decreases from approximately 81% to 25%. In addition, the proportions of Mg in the two sets of films are roughly the same at equal evaporation source temperatures of magnesium.

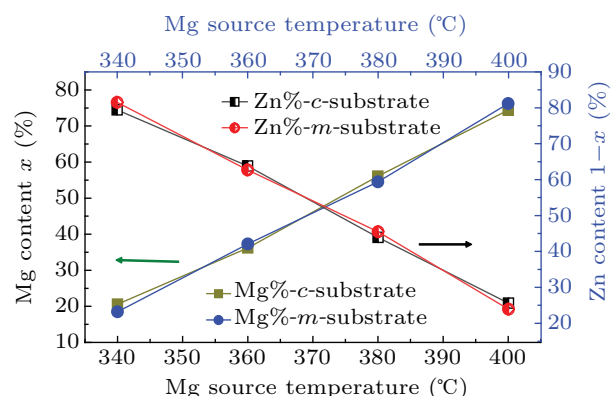


Fig. 1. Mg content of the  $\text{Zn}_{1-x}\text{Mg}_x\text{O}$  films from EDS.

Figures 2(a) and 2(b) show the XRD (Rigaku, Japan) results from the  $\text{Zn}_{1-x}\text{Mg}_x\text{O}$  alloy films grown on the *c*-ZnO substrate with different Mg contents using a Cu  $K\alpha$  radiation source (1.54056 Å). The black curved lines are from the substrates as a comparison to the films. Apparently, the alloy films grown on the *c*-plane (0001) ZnO substrate show a peak of cubic phase MgO with an Mg content between 20.6% and 56.1%, as shown by the black arrow in Fig. 2(a); this result is indicative of the appearance of phase separation. Figure 2(b) presents an amplified image of the rectangular area in Fig. 2(a), which shows that as the Mg content increases, there is a slight increase in the MgO (002) peak and a shift in the peak position from 42.4° to 42.6°, as marked by the black circles and dashed line. This result indicates an increase in the proportion of the cubic phase with a decrease in the lattice length from 4.24 Å to 4.26 Å as the Mg content increases. Moreover, the XRD result reveals a (111) orientation of the cubic phase at 36.8° when the Mg content reaches 74.4%, as labeled by the blue arrow in Fig. 2(b). This phenomenon reflects that the Mg content of 74.4% is able to trigger multiple growth orientations of the cubic phase for the alloy film on the *c*-substrate. Furthermore, the (002) peak of the cubic phase splits into two peaks. One is at 42.1° and the other at 42.8°, as marked by the red arrows in Fig. 2(b), corresponding to the  $\text{Zn}_{1-x}\text{Mg}_x\text{O}$  phase with a cubic structure and bulk-like cubic MgO, respectively. Therefore, at an Mg content of 74.4%, the alloy film exhibits an interesting feature of 2nd-order phase separation. Regarding the  $\text{Zn}_{1-x}\text{Mg}_x\text{O}$  alloy films grown on the *m*-substrate, it is remarkable that no phase separation is observed for the Mg content at 18.5% (shown with a red curve in Fig. 2(c)). When the Mg content reaches 37.3% (shown with a blue curve in Fig. 2(c)), an obvious (002) peak and weaker (022) peak of the cubic phase start to appear in Fig. 2(c). Similar to the case of the alloy films grown on the *c*-ZnO substrate,

the intensities of the (002) and (022) peaks related to the cubic phase increase with an increasing Mg content, accompanied by slight shifts in the peak positions, as labeled by the black circles and dashed lines in Fig. 2(d); this result is shown by the

amplified image of the area marked by the black rectangle in Fig. 2(c). It is obvious that the Mg content promotes the phase separation as well as a new orientation of the cubic phase in the alloy film.

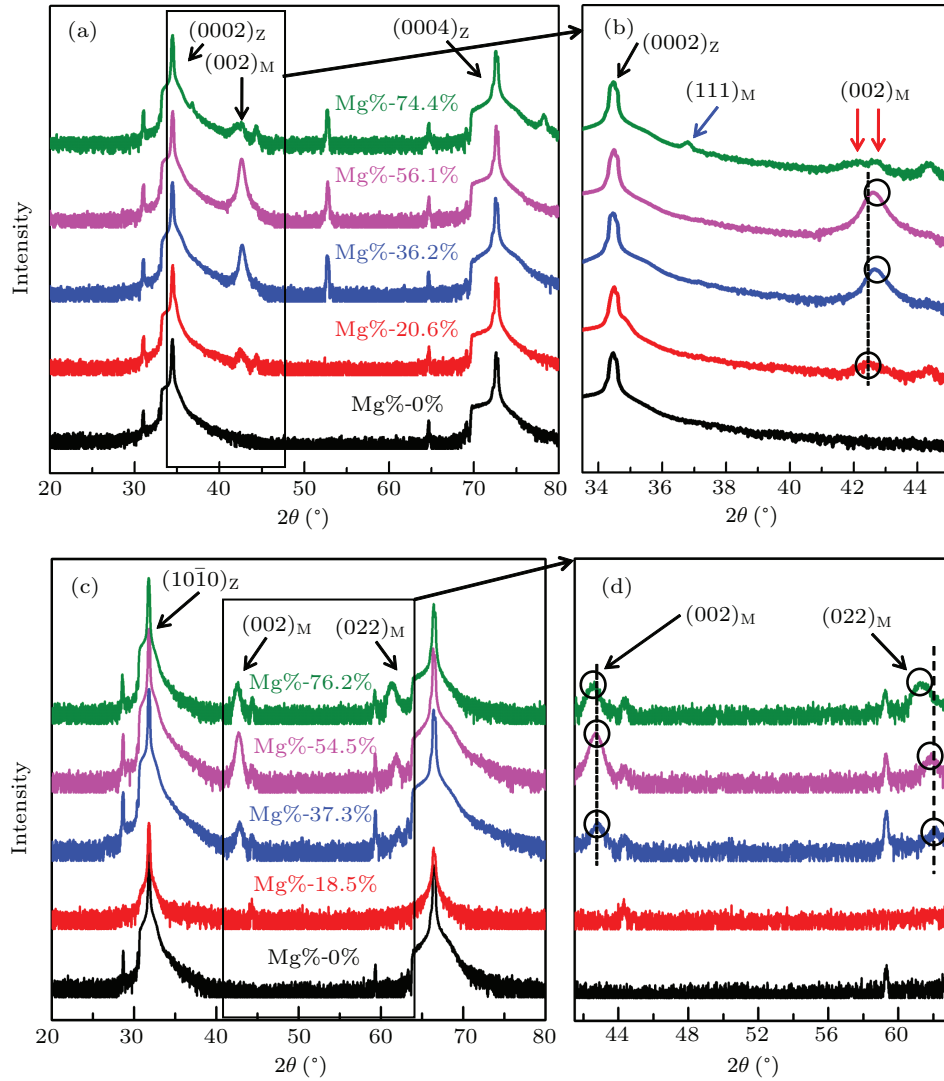


Fig. 2. XRD results from the  $\text{Zn}_{1-x}\text{Mg}_x\text{O}$  alloy films with different Mg contents grown on the *c*-ZnO substrate (a), (b) and *m*-ZnO substrate (c), (d).

To obtain the interfacial relationships between the cubic phases and substrates, we characterized the alloy films using XRD phi scan mode. Figure 3(a) shows the phi scan images of  $\text{MgO}\{111\}$  crystal plane diffraction with  $\chi = 54^\circ$  and  $2\theta = 39.3^\circ$  and those of  $\text{ZnO}\{10\bar{1}1\}$  crystal plane diffraction with  $\chi = 61^\circ$  and  $2\theta = 36.2^\circ$ , as shown by the red and blue curves, respectively. It is well known that the phi scan image of  $\text{ZnO}\{10\bar{1}1\}$  planes from the  $\text{ZnO}[0002]$  azimuth substrate is composed of six peaks:  $(10\bar{1}1)_Z$ ,  $(01\bar{1}1)_Z$ ,  $(\bar{1}101)_Z$ ,  $(\bar{1}011)_Z$ ,  $(01\bar{1}1)_Z$ , and  $(1\bar{1}01)_Z$ , as illustrated in Fig. 3(a). These six peaks reflect the sixfold symmetry of  $[0002]$  azimuth ZnO. Detailed explanations can be found in our previous work.<sup>[28]</sup> Regarding the  $[002]$  azimuth MgO, the phi scan image of  $\{111\}$ -MgO should be composed of four peaks:  $(111)_M$ ,  $(\bar{1}\bar{1}1)_M$ ,  $(\bar{1}\bar{1}1)_M$ , and  $(1\bar{1}1)_M$ . Here,

the Z and M subscripts represent ZnO and MgO, respectively. However, the phi scan image of the  $\{111\}$ -MgO plane from the alloy film shows 12 peaks, as shown by the blue curve in Fig. 3(a). This result indicates that a cubic phase MgO film is embedded in the alloy film with the  $[002]$  orientation, which becomes a sixfold symmetric in-plane structure via a rotation of  $120^\circ$ . These structures are named c-variation I, c-variation II, and c-variation III, and are abbreviated as c-v-I, c-v-II, and c-v-III, respectively. Here, we define the first peak to be from the  $(111)_{\text{MgO-c-v-I}}$  crystal plane diffraction. Based on the relationships of the rotations among the three kinds of variants, it is not difficult to calculate that the other peaks are from  $(\bar{1}\bar{1}1)_{\text{M-c-v-II}}$ ,  $(\bar{1}\bar{1}1)_{\text{M-c-v-III}}$ ,  $(\bar{1}\bar{1}1)_{\text{M-c-v-I}}$ ,  $(1\bar{1}1)_{\text{M-c-v-II}}$ ,  $(1\bar{1}1)_{\text{M-c-v-III}}$ ,  $(1\bar{1}1)_{\text{M-c-v-I}}$ ,  $(111)_{\text{M-c-v-II}}$ ,  $(111)_{\text{M-c-v-III}}$ ,  $(111)_{\text{M-c-v-I}}$ ,  $(\bar{1}\bar{1}1)_{\text{M-c-v-II}}$ ,



and  $(111)_{M-c-v-III}$  crystal plane diffractions, respectively, as illustrated in Fig. 3(a). It is clearly seen that the  $\phi$  angles of  $(10\bar{1}1)_Z$ ,  $(01\bar{1}1)_Z$ ,  $(\bar{1}101)_Z$ ,  $(\bar{1}011)_Z$ ,  $(01\bar{1}1)_Z$ , and  $(1\bar{1}01)_Z$  are nearly identical to those of  $(111)_{M-c-I}$ ,  $(\bar{1}\bar{1}1)_{M-c-v-III}$ ,  $(1\bar{1}1)_{M-c-v-II}$ ,  $(\bar{1}\bar{1}1)_{M-c-v-I}$ ,  $(1\bar{1}1)_{M-c-v-III}$ , and  $(\bar{1}\bar{1}1)_{M-c-v-II}$ , respectively, thereby indicating  $[10\bar{1}0]_Z \parallel [110]_M$ . Based on the discussions above, we can obtain the following interfacial relationship between the

cubic phase film and the substrate:

$$\begin{aligned} [110][\bar{1}\bar{1}0](002)_{M-c-v-I} &\parallel [10\bar{1}0][\bar{1}2\bar{1}0](0001)_Z; \\ [110][\bar{1}\bar{1}0](002)_{M-c-v-II} &\parallel [\bar{1}\bar{1}20][1\bar{1}00](0001)_Z; \\ [110][\bar{1}\bar{1}0](002)_{M-c-v-III} &\parallel [2\bar{1}\bar{1}0][01\bar{1}0](0001)_Z. \end{aligned}$$

According to these interfacial relationships, we can draw the atomic model from the top view, as shown in Fig. 3(b).

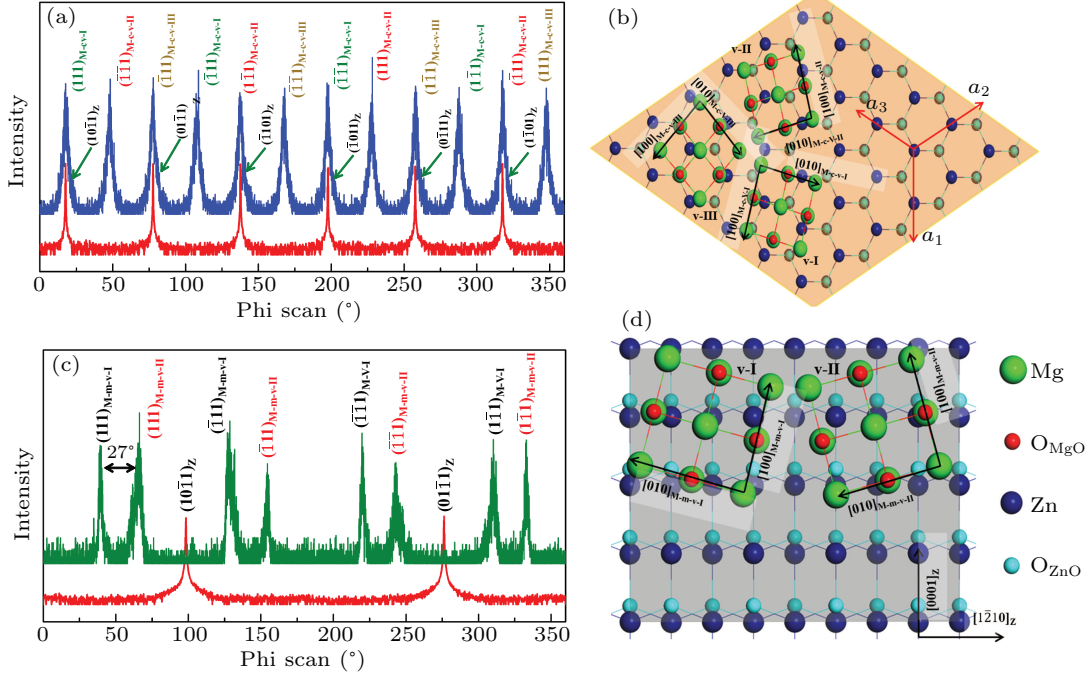


**Fig. 3.** XRD  $\phi$  scan results and atomic models from the top view for the  $Zn_{1-x}Mg_xO$  alloy films grown on the  $c$ -ZnO substrate (a), (b) and  $m$ -ZnO substrate (c), (d).

The red and green curves in Fig. 3(c) show the  $\phi$  scan images from the  $m$ -ZnO substrate (red) and the cubic phase film (green), respectively. The  $\phi$  scan of the substrate with  $\chi = 60^\circ$  and  $2\theta = 36.2^\circ$  provides  $(10\bar{1}1)_Z$  and  $(01\bar{1}1)_Z$  plane diffraction peaks, as labeled in Fig. 3(c). The  $\phi$  scan of the film displays the  $\{111\}$ -MgO plane peaks from the cubic phase MgO ebbbed in the alloy films with  $\chi = 54^\circ$  and  $2\theta = 39.2^\circ$ . Therefore, theoretically, the green curve should show four peaks, namely, the  $(111)$ -MgO,  $(\bar{1}\bar{1}1)$ -MgO,  $(\bar{1}\bar{1}1)$ -MgO, and  $(\bar{1}\bar{1}1)$ -MgO crystal plane diffractions, as illustrated in Fig. 4(b). Nevertheless, in fact, the green curve shows two sets of diffraction peaks, and the angle of the two variants is approximately  $27^\circ$ , indicating the existence of two rotational domains of the  $(002)_M$  cubic phase, which are named  $m$ -variants I and II and are abbreviated  $m$ -v-I and  $m$ -v-II, respectively. Again, we define the first peak to be from  $(111)_{M-m-v-I}$ . Therefore, the other peaks can be calculated to be from  $(111)_{M-m-v-II}$ ,  $(\bar{1}\bar{1}1)_{M-m-v-I}$ ,  $(\bar{1}\bar{1}1)_{M-m-v-II}$ ,  $(1\bar{1}1)_{M-m-v-I}$ ,  $(1\bar{1}1)_{M-m-v-II}$ ,  $(\bar{1}\bar{1}1)_{M-m-v-I}$ , and  $(\bar{1}\bar{1}1)_{M-m-v-II}$ , as illustrated in Fig. 3(c). In addition, from the  $\phi$  scan in Fig. 3(c), we can see that the angle between

$(111)_{M-m-v-I}$  and  $(10\bar{1}1)_Z$  and that between  $(111)_{M-m-v-II}$  and  $(10\bar{1}1)_Z$  equal approximately  $60^\circ$  and  $33^\circ$ , respectively. The projections of normal of the  $(1\bar{1}00)_Z$  and  $(01\bar{1}0)_Z$  crystal planes on the  $(10\bar{1}0)$  plane are along the  $[\bar{1}2\bar{1}0]_Z$  and  $[\bar{1}\bar{2}10]_Z$  azimuths, respectively, and detailed explanations can be found in our previous work.<sup>[25]</sup> From the angle relationship between MgO and the substrate planes, we obtain the interfacial relationships as follows:

$$\begin{aligned} [110][\bar{1}\bar{1}0](002)_{M-m-v-I} &\parallel [\bar{1}2\bar{1}1][\bar{5}10\bar{5}1](10\bar{1}0)_Z; \\ [110][\bar{1}\bar{1}0](002)_{M-m-v-II} &\parallel [\bar{5}10\bar{5}2][\bar{1}2\bar{1}\bar{1}](10\bar{1}0)_Z. \end{aligned}$$

Moreover, from these interfacial relationships, we can draw the atomic models from a side view, as illustrated in Fig. 3(d). To investigate the nanoscale features of the film phases as well as the interface, TEM measurements were performed on the samples with the highest Mg content.

#### 4. TEM and SAED results and discussion

Figure 4(a) is a low magnification TEM image from the  $Zn_{1-x}Mg_xO$  alloy film on the  $c$ -ZnO substrate, showing a thickness of approximately 350 nm, as labeled by the blue

double arrow. Here, the red dashed lines mark the interfaces between the  $\text{Zn}_{1-x}\text{Mg}_x\text{O}$  film and the substrate. Numerous grain boundaries clearly exist, as labeled by the yellow dashed curves in Fig. 4(a). This result can be further verified by the higher magnification TEM image, as marked by the yellow dashed curves in Fig. 4(e). Interestingly, we found a superlattice-like structure localized in certain areas of the film, as labeled by the red rectangles in Fig. 4(c). This result can be further demonstrated by the high-resolution TEM images in Fig. 4(d). It is speculated that phase separation induces polycrystalline structures with numerous grains and grain boundaries. On the other hand, the lower growth temperature hinders sufficient reaction between O and Zn. As a result, new superlattice-like structures appear in the grains due to vacancies (shown in Fig. 4(d)). In fact, this phenomenon has been found in the  $\text{SrRuO}_3$  films prepared by pulsed laser deposition.<sup>[29]</sup> Figure 4(b) shows a selected area electron diffraction (SAED) pattern from the corresponding area including both the substrate and film. Three sets of diffraction patterns clearly exist. One is from the  $c$ -ZnO substrate along the  $[\bar{1}210]_Z$  azimuth, as labeled by the red circles and red arrows. The other two are from the cubic phase films, one from the  $[001]_M$  orientation component along the  $[110]_M$  azimuth, as labeled by the

yellow circles, indicating  $[110](001)_M \parallel [\bar{1}210](0001)_Z$ , which is consistent with the analysis results of the XRD phi scan for the film on the  $c$ -substrate; the other is from the  $[111]_M$  orientation component along the  $[\bar{1}2\bar{1}]_M$  azimuth, as labeled by the green circles in Fig. 4(b). In addition, we calculated  $(a[\bar{1}01])^*/(a[\bar{1}\bar{1}\bar{1}])^*$  to be approximately 2.88, as labeled by the green arrow, reflecting that  $a[\bar{1}\bar{1}\bar{1}]/a[\bar{1}01]$  equals 2.88, which is larger than the theoretical value of 2.43. This result hints that the film of the  $[111]_M$  orientation belongs to a pseudocubic phase. Figure 4(e) is a high-resolution TEM image, showing the structures of the two growth orientations, as labeled by the yellow dashed curve. The yellow arrow in Fig. 4(e) represents the film growth orientation. Figures 4(f) and 4(h) correspond to the amplified images of the two areas labeled by the blue and red rectangles in Fig. 4(e). The region in Fig. 4(f) shows a rectangular feature with lattice lengths of 2.7 Å and 7.4 Å, as labeled by blue arrows, which are close to the theoretical lattice lengths of the  $(\bar{1}21)$ -MgO plane. In addition,  $a[\bar{1}\bar{1}\bar{1}]/a[\bar{1}01]$  is calculated to be 2.74, which is slightly larger than the theoretical values ( $a[\bar{1}\bar{1}\bar{1}] = 7.3$  Å and  $a[\bar{1}\bar{1}\bar{1}] = 3.0$  Å) and is consistent with the SAED results from Fig. 4(b). This feature suggests that this region belongs to the MgO- $(\bar{1}21)$  plane structure with a  $[111]_M$  azimuth orientation. This

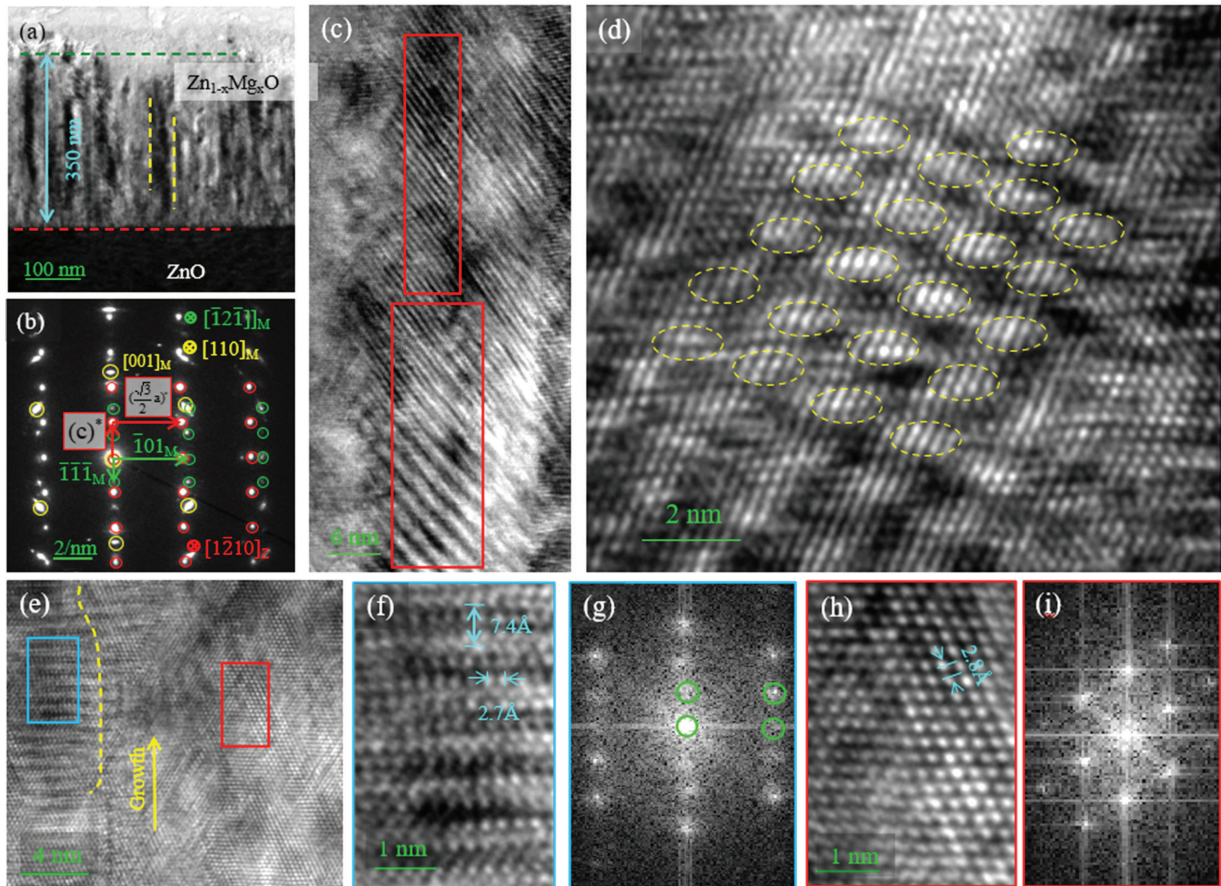


**Fig. 4.** TEM image of the alloy film grown on the  $c$ -ZnO substrate: (a) low magnification TEM image; (b) the corresponding SAED; (c), (d) HRTEM images of the film, showing the superlattice-like structure in some areas, as marked by the red rectangle in image (c) and the yellow circle in image (d); (e) HRTEM image showing two regions separated by the yellow dashed line. (f), (h) The corresponding enlarged images of the two areas marked by the blue and red rectangles in (e); and (g), (i) the corresponding FFT images from (f), (h).



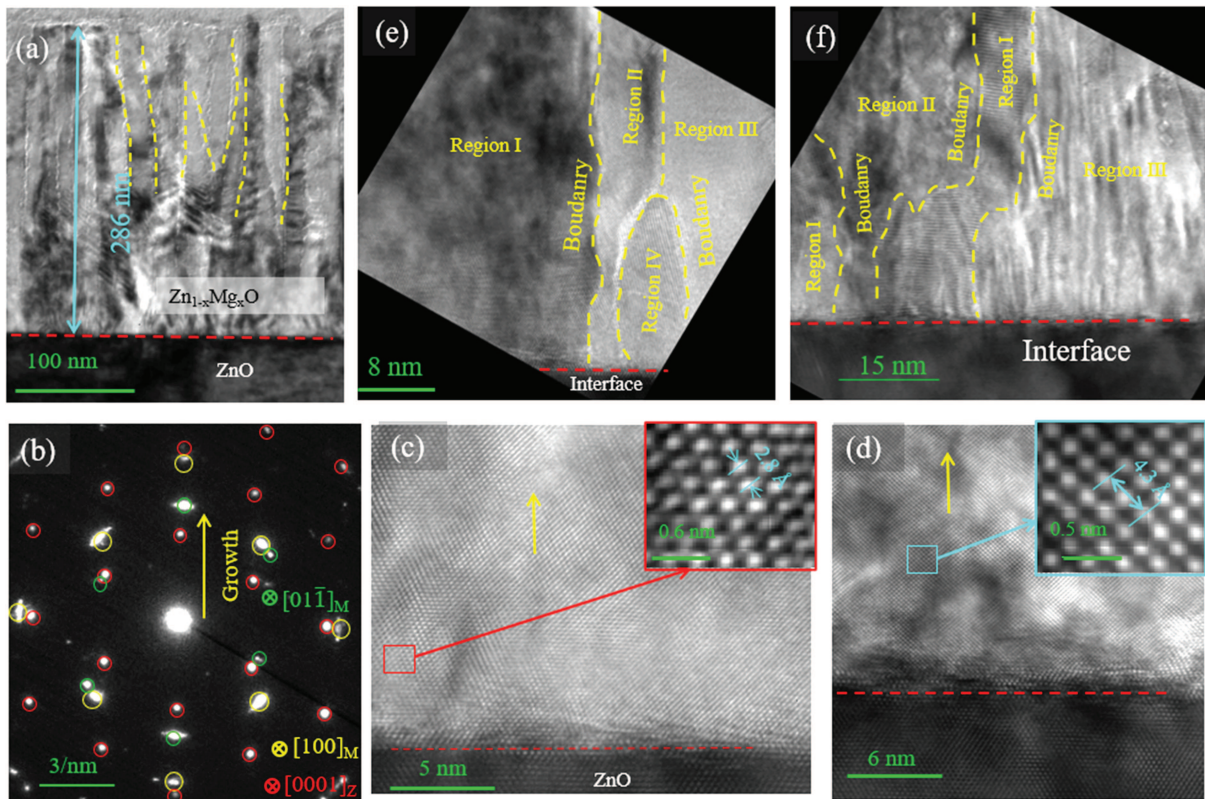
result can be further confirmed by the corresponding fast Fourier transform (FFT) image, as shown in Fig. 4(g). The FFT image displays a rectangular spot array, as illustrated by the green circles, similar to the diffraction spot arrays along the  $[1\bar{2}1]_M$  azimuth, as marked by the green spot arrays in Fig. 4(b). Figure 4(h) displays a rhombus lattice structure with distances of 2.8 Å between the nearest neighbor atoms, which is also slightly larger than the theoretical value of 2.6 Å. The corresponding FFT image (see Fig. 4(i)) shows a hexagonal spot array. This feature suggests that the region of Fig. 4(h) shows the MgO-(110) plane structure with the  $[001]_M$  azimuth orientation. Notably, the lattice lengths of the cubic phase are smaller than the bulk values, indicating the high possibility that the cubic crystal structure is for the  $Zn_{1-x}Mg_xO$  alloy instead of pure MgO.

Figure 5(a) is a low magnification image of the  $Zn_{1-x}Mg_xO$  film on the  $m$ -ZnO substrate, showing a thickness of approximately 286 nm. Similar to the film grown on the  $c$ -ZnO substrate, the film exhibits numerous grain boundaries, as labeled by the yellow dashed lines in Figs. 5(a), 5(e), and 5(f). Figure 5(b) corresponds to the SAED pattern captured along the  $[0001]_Z$  azimuth, as labeled by the red circles. Again, the yellow arrow represents the growth orientation. Apparently, one can find that, in addition to the hexagonal structure of the substrate, the SAED image simultaneously displays two other sets of diffractions from the cubic phase with the  $[011]$  ori-

entation; one is captured along the  $[100]_M$ , as labeled by the yellow circles, and the other is captured along the  $[01\bar{1}]_M$  azimuth, as labeled by the green circles. These results indicate that the interfacial relationships between the  $[011]$  orientation film and the  $m$ -ZnO substrate are as follows:

$$\begin{aligned} [100][0\bar{1}1](011)_{M-I} &\parallel [0001][1\bar{2}10](10\bar{1}0)_Z; \\ [01\bar{1}][100](011)_{M-II} &\parallel [0001][1\bar{2}10](10\bar{1}0)_Z. \end{aligned}$$

Figures 5(c) and 5(d) show the high-resolution (HR) TEM images from two different regions. These images show that the film interface is very sharp without visible dislocations, as indicated by the red dotted line. The insets of the upper right corner correspond to the amplified images of the areas marked by the red rectangle in Fig. 5(c) and blue rectangle in Fig. 5(d). From the structural relationship and the lattice lengths between the two nearest neighbor atoms in Figs. 5(c) and 5(d), we can calculate the lattice length  $a_M$  to be 4.6 Å and 4.3 Å, respectively. Both results are slightly larger than the theoretical values, which is similar to the case of the  $c$ -ZnO substrate. It is worth pointing out that compared with that from Fig. 5(c), the larger lattice length from Fig. 5(d) originates from the phenomenon that the  $[01\bar{1}]_M$  azimuth is not parallel to the  $[0001]_Z$  azimuth, thereby leading to a small deviation. In fact, the distorted hexagonal spot arrays in the corresponding SAED pattern (Fig. 5(b)) also reflect this result.



**Fig. 5.** TEM images of the alloy film grown on the  $m$ -ZnO substrate: (a) low magnification image of the film on the  $m$ -ZnO substrate. (b) Corresponding SAED of (a). (c), (d) HRTEM images of two different areas. The illustrations in the upper right corners of (c), (d) correspond to the enlarged image of the area, as shown by the red and blue rectangles in (c) and (d), respectively. (e), (f) Two different areas grown on the  $m$ -ZnO substrate. The HRTEM image of the thin film shows many grain boundaries, which are indicated by the yellow dashed curves.

## 5. Conclusion

In this work, a plasma-assisted MBE method was used to prepare  $\text{Zn}_{1-x}\text{Mg}_x\text{O}$  thin films on the polar  $c$ -plane (0001) and nonpolar  $m$ -plane (10 $\bar{1}$ 0) ZnO substrates. The contents of zinc and magnesium in the  $\text{Zn}_{1-x}\text{Mg}_x\text{O}$  films were determined by EDS. XRD and HRTEM were used to analyze the growth orientations of the  $\text{Zn}_{1-x}\text{Mg}_x\text{O}$  film and the interface between the film and substrate. Various characterization data show that under the same growth conditions, the  $\text{Zn}_{1-x}\text{Mg}_x\text{O}$  films grown on the polar and nonpolar substrates exhibit different phase evolutions as the Mg content increases. In particular, the alloy films start to show cubic phases when the Mg content is 20% and 37% for the alloy films grown on  $c$ -ZnO and  $m$ -ZnO, respectively. No hexagonal phases are observed from the HRTEM images for the alloy films at an Mg content of more than 70%. Interestingly, the cubic phases exhibit three-fold and two-fold rotational domains for the alloy films grown on the  $c$ -ZnO and  $m$ -ZnO substrates, respectively. The influence of polar and nonpolar substrates on the phase separation of thin films can provide a good reference for other studies.

## Acknowledgement

We are grateful to the members of the MBE laboratory of the Department of Physics, Xiamen University for their help and discussion.

## References

- [1] Özgür, Alivov Y I, Liu C, Teke A, Reshchikov M A, Doğan S, Avrutin V, Cho S J and Morkoç H 2005 *J. Appl. Phys.* **98** 041301
- [2] Wang K, Li L and Yao S D 2009 *Chin. Phys. Lett.* **26** 108101
- [3] Etacheri V, Roshan R and Kumar V 2012 *ACS Applied Materials & Interfaces* **4** 2717
- [4] Vashaei Z, Minegishi T, Suzuki H, Hanada T, Cho M W, Yao T and Setiawan A 2005 *J. Appl. Phys.* **98** 054911
- [5] Maity S and Sahu P P 2019 *Thin Solid Films* **674** 107
- [6] Wang L K, Ju Z G, Shan C X, Zheng J, Li B H, Zhang Z Z, Yao B, Zhao D X, Shen D Z and Zhang J Y 2010 *Journal of Crystal Growth* **312** 875
- [7] Han S, Shen D Z, Zhang J Y, Zhao Y M, Jiang D Y, Ju Z G, Zhao D X and Yao B 2010 *Vacuum* **84** 1149
- [8] Xu T N, W H Z, Qiu D J and Chen N B 2003 *Chin. Phys. Lett.* **20** 1829
- [9] Takeuchi I, Yang W, Chang K S, Aronova M A, Venkatesan T, Vispute R D and Bendersky L A 2003 *J. Appl. Phys.* **94** 7336
- [10] Wei M, Boutwell R C, Mares J W, Scheurer A and Schoenfeld W V 2011 *Appl. Phys. Lett.* **98** 261913
- [11] Yadav M K, Ghosh M, Biswas R, Raychaudhuri A K, Mookerjee A and Datta S 2007 *Phys. Rev. B* **76** 195450
- [12] Wu K P, Qi J, Peng B, Tang K, Ye J D, Zhu S M and Gu S L 2015 *Acta Phys. Sin.* **64** 187304 (in Chinese)
- [13] Liang J, Wu H Z, Lao Y F, Qiu D J, Chen N B and Xu T N 2004 *Chin. Phys. Lett.* **21** 1135
- [14] Boutwell R C, Wei M, Baudelet M and Schoenfeld W V 2014 *J. Alloys Compd.* **584** 327
- [15] Wu Y, Dong B, Zhang L, Song H B and Yan C J 2018 *International Journal of Hydrogen Energy* **43** 12627
- [16] Santander-Syro A F, Copie O, Kondo T, Fortuna F, Pailhes S, Weht R, Qiu X G, Bertran F, Nicolaou A, Taleb-Ibrahimi A, Le Fevre P, Herranz G, Bibes M, Reyren N, Apertet Y, Lecoer P, Barthelemy A and Rozenberg M J 2011 *Nature* **469** 189
- [17] Haeni J H, Irvin P, Chang W, Uecker R, Reiche P, Li Y L, Choudhury S, Tian W, Hawley M E, Craigo B, Tagantsev A K, Pan X Q, Streiffer S K, Chen L Q, Kirchoefer S W, Levy J and Schlom D G 2004 *Nature* **430** 758
- [18] Zhang S G, Guo D L, Wang M J, Javed M S and Hu C G 2015 *Applied Surface Science* **335** 115
- [19] Ueno K, Nakamura S, Shimotani H, Ohtomo A, Kimura N, Nojima T, Aoki H, Iwasa Y and Kawasaki M 2008 *Nat. Mater.* **7** 855
- [20] Park M H, Lee H J, Kim G H, Kim Y J, Kim J H, Lee J H and Hwang C S 2011 *Adv. Funct. Mater.* **21** 4305
- [21] Zhu Y M, Chang W S, Yu R, Liu R R, Wei T C, He J H, Chu Y H and Zhan Q 2015 *Appl. Phys. Lett.* **107** 191902
- [22] Liang D D, Li X P, Wang J S, Wu L C and Chen P 2018 *Solid-State Electronics* **145** 46
- [23] Fritsch D, Schmidt H and Grundmann M 2006 *Appl. Phys. Lett.* **88** 134104
- [24] Pintilie I, Pasuk I, Ibanescu G A, Negrea R, Chirila C, Vasile E and Pintilie L 2012 *J. Appl. Phys.* **112** 104103
- [25] Zheng P P, Sun B, Chen Y Z, Elshekh H, Yu T, Mao S S, Zhu S H, Wang H Y, Zhao Y and Yu Z 2019 *Applied Materials Today* **14** 21
- [26] Zheng H, Zhu H, Tang Z, Wang Y, Wei H and Shan C 2020 *Chin. Phys. B* **29** 097302
- [27] Hu Z F, W H H, Lv Y W and Zhang X Q 2015 *Chin. Phys. B* **24** 107302
- [28] Zhou H, Wang J, Mai M F, Ma X Z, Hu S J, Xu M C, Bai L H and Yan S S 2020 *Thin Solid Films* **709** 138074
- [29] Maria J P, Trolrier-McKinstry S, Schlom D G, Hawley M E and Brown G W 1998 *J. Appl. Phys.* **83** 4373